

SIMULATION OF NAPTF HIGH TIRE PRESSURE TESTS WITH ADVANCED FINITE
ELEMENT MODELING

By:

Hao Wang, Ph.D. and Maoyun Li
Department of Civil and Environmental Engineering
Rutgers, The State University of New Jersey
Piscataway, NJ 08854
Phone: (848) 445-2814; Fax: (732) 445-0517
hwang.cee@rutgers.edu
ml929@scarletmail.rutgers.edu

Navneet Garg, Ph.D.
Project Manager, ANG-E262
Airport Pavement R&D Section,
William J. Hughes Technical center
Atlantic City Intl. Airport, NJ 08405
Phone: 609-4854483; Fax: 609-4854845
Navneet.Garg@faa.gov

PRESENTED FOR THE
2014 FAA WORLDWIDE AIRPORT TECHNOLOGY TRANSFER CONFERENCE
Galloway, New Jersey, USA

August 2014

ABSTRACT

The new generation of aircrafts, like Boeing 787 and Airbus 350/380, has tire pressure exceeding 1.5MPa. This creates a challenge for the traditional PCN rating with 1.5MPa limitation. A series of high tire pressure tests on heated pavements have been conducted at the National Airport Pavement Test Facility (NAPTF) to duplicate the worst-case conditions likely to be encountered in the field. This paper aims to evaluate the effect of high aircraft tire pressure on asphalt pavement responses using three-dimensional (3-D) finite element (FE) modeling. The FE model characterized the hot-mix asphalt (HMA) layer as a viscoelastic material and utilized an implicit dynamic analysis to predict the time-dependent pavement responses under moving aircraft tire loading. The tire loading was simulated as a continuously moving load having half-sinusoidal shape distribution along the contact length and non-uniform distribution along five ribs of the tire. The pavement responses (tensile, shear and compressive stresses/strains) under various loading conditions were calculated and compared. Two temperature profiles were considered in the analysis; one is the "artificial" bottom-up heating that was used in the NAPTF full-scale test and another one is the "natural" top-down heating. The results show that the critical pavement responses increase by 10 to 20% as the tire inflation pressure increases from 1.45 to 1.69MPa, depending on the type of pavement response. The analysis findings can support the NAPTF high tire pressure test results and provide valuable suggestions for airfield pavement design under heavy aircrafts with high tire pressure.

INTRODUCTION

The deterioration of pavement performance is significantly affected by loading factors, such as the magnitude and frequency of load, tire pressure, and tire-pavement contact stresses. Many studies have been conducted to analyze the effects of loading factors on highway and airfield pavement responses. For example, increasing tensile strains at the bottom of the AC layer was found as the truck tire inflation pressure increased, which resulted in decreasing pavement life [1]. Compared to truck tires, aircraft tires carry much greater wheel loads with a much higher tire inflation pressure. Therefore, it is expected that the increase of tire pressure may accelerate airfield pavement deterioration.

Aircraft tire inflation pressure ranges from 1.2-1.5MPa (174-217psi) depending on aircraft gross weights and landing gear configurations. However, the new generations of aircrafts, like Boeing 787 and Airbus 350/380, have tire pressures exceeding 1.5MPa (217psi). This creates a challenge for the traditional Pavement Classification Number (PCN) rating that includes four pressure categories: W (no pressure limitation), X (1.5MPa [217psi] limitation), Y (1.0MPa [145psi] limitation), and Z (0.5MPa [72psi] limitation) [2]. Field measurements have found that the vertical contact stresses under the edge ribs of aircraft tires could be as high as 1.5-3 times the inflation pressure, depending on the load applied on the tire [3, 4, 5, 6].

A series of full-scale tests have been conducted at the National Airport Pavement Test Facility (NAPTF) to evaluate pavement responses under aircraft loading. Accelerated testing at NAPTF shows that the rutting and upheaval in a conventional flexible pavement on medium-strength subgrade were mainly attributed to shear failure in the base, subbase and subgrade [7, 8]. Garg and Hayhoe [9] found that the asphalt concrete strain responses were strongly affected by the pavement temperature and loading speed. Recently, high tire pressure tests were performed at the NAPTF. Roginski [10] found that the rutting in the asphalt layer was the main failure mode under heavy aircraft loading, and high tire pressure had no adverse effect on

flexible pavements that have stable asphalt layers and meet thickness requirement. Fabre et al. [11] emphasized the importance of considering non-uniform contact stress distribution in the analysis of high tire pressure effect on pavement responses in the upper layer.

OBJECTIVE AND SCOPE

This paper aims to evaluate the effect of high aircraft tire pressure on asphalt pavement responses using three-dimensional (3-D) finite element (FE) modeling. An existing asphalt pavement section at the NAPTF was used in the analysis. This FE model characterized the hot-mix asphalt (HMA) layer as a viscoelastic material and utilized an implicit dynamic analysis to predict the time-dependent pavement responses under moving aircraft tire loading. The tire loading was simulated as a continuously moving load with a half-sinusoidal distribution along the contact length and a non-uniform distribution along the five ribs of the tire. Two different temperature profiles were considered in the analysis. The pavement responses (tensile, compressive and shear strains) under different loading conditions were calculated and compared. The rutting depths were predicted using two different mechanistic-empirical performance models.

PAVEMENT STRUCTURE AND MATERIAL CHARACTERIZATION

The modeled pavement structure is an existing section built in the NAPTF in the Boeing high tire pressure test program, as shown in Fig. 1. The pavement section consists of a HMA wearing surface layer, an Eco-concrete base layer (P306), an uncrushed aggregate subbase layer (P154), and the subgrade. The dynamic modulus of the HMA and the elastic modulus of base/subbase layers and subgrade were provided by FAA NAPTF.

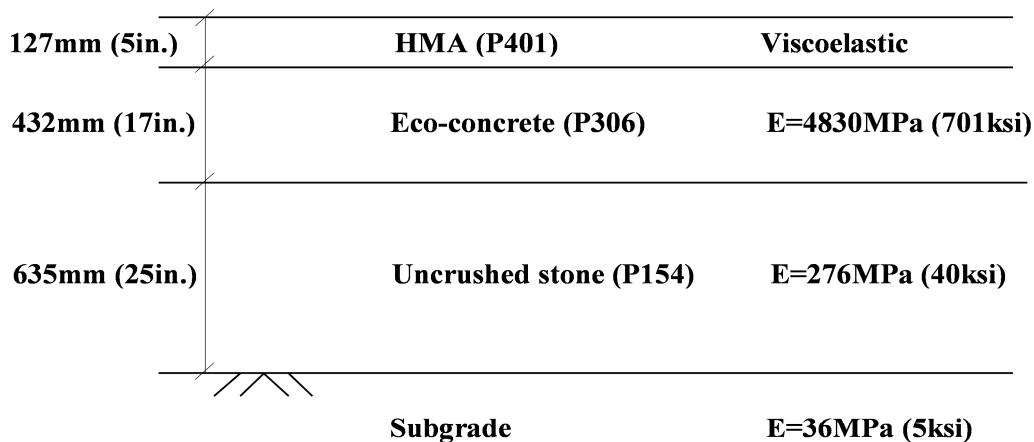


Figure 1. Cross-Section of the Modeled Pavement Structure

Fig. 2 shows the measured dynamic modulus and the fitted master curve using the sigmoid function at a reference temperature of 20°C (68°F). As expected, under a constant loading frequency, the dynamic modulus decreases as the temperature increases; and under a constant testing temperature, the dynamic modulus increases as the frequency increases.

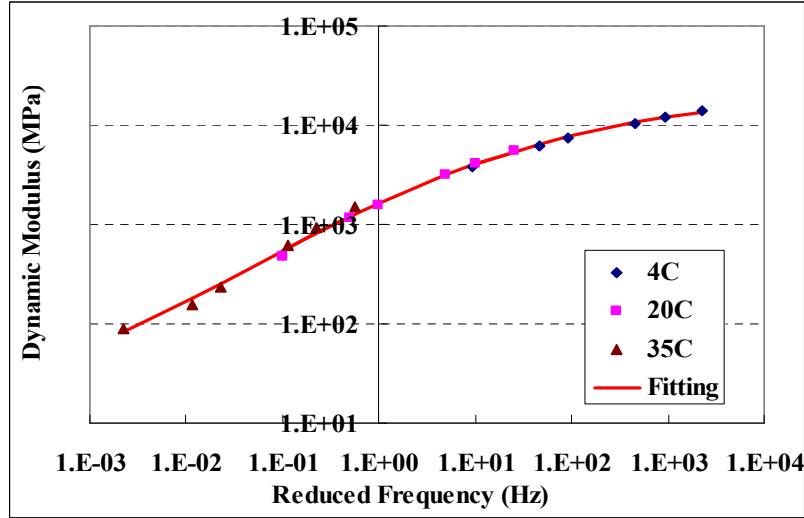


Figure 2. Master Curve of Dynamic Modulus

The relaxation modulus was inter-converted from the dynamic modulus using Eq. 1 and Eq. 2 assuming that the linear viscoelasticity of HMA was represented by a generalized Maxwell solid model [12]. The relaxation modulus and relaxation times were determined by minimizing the sum of squares of the errors (Eq. 3). The solver function in EXCEL was used to perform the curve fitting in an iterative process. The bulk and shear relaxation moduli were calculated assuming a constant Poisson's ratio.

$$E'(\omega) = E_{\infty} + \sum_{i=1}^n \frac{\omega^2 \tau_i^2 E_i}{1 + \omega^2 \tau_i^2} \quad (1)$$

$$E''(\omega) = \sum_{i=1}^n \frac{\omega \tau_i E_i}{1 + \omega^2 \tau_i^2} \quad (2)$$

$$\min \sum_{j=1}^k \left[\left(\frac{E'(\omega)_{\text{calculated}}}{E'(\omega)_{\text{measured}}} - 1 \right)^2 + \left(\frac{E''(\omega)_{\text{calculated}}}{E''(\omega)_{\text{measured}}} - 1 \right)^2 \right] \quad (3)$$

where:

$E'(\omega)$ is real part of the dynamic modulus;

$E''(\omega)$ is imaginary part of the dynamic modulus;

E_{∞} is equilibrium relaxation modulus at infinite time;

ω is angular frequency;

E_i , and τ_i are Prony series parameters for relaxation modulus;

n is number of Maxwell elements; and

k is number of data points from the measurements.

Figure 3 plots the measured temperature profile in the asphalt layer along with the reversed temperature profile. The measured temperature profile was obtained from the "artificial" bottom-up heating that was used in the full-scale test; while the reversed one represents the "natural" top-down heating under sunlight.

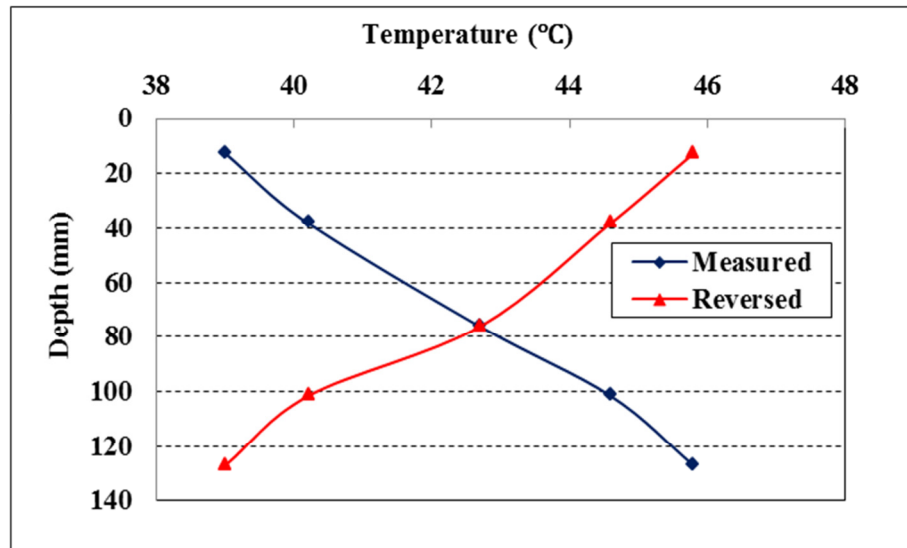


Figure 3. Two Temperature Profiles in FE Modelling

SIMULATION OF TIRE LOADING

The applied tire loads in the full-scale test were 272.7kN (61.3kips) and 233.5kN (52.5 kips), which are approximately equivalent to the load per landing wheel of A380 with the total weight of 586 tons and 502 tons. Two pressure levels (1.45MPa [210psi] and 1.69MPa [245psi]) were used to evaluate the influence of tire inflation pressure on pavement responses due to the advent of new aircrafts exceeding the current ICAO tire pressure limit in category X (1.5MPa [217psi]). For each tire inflation pressure, non-uniform contact stress distributions were assumed in the tire imprint area with five ribs, as shown in Fig. 4.

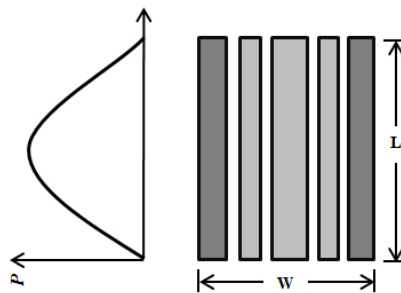


Figure 4. Non-uniform Contact Stress Assumptions

The non-uniform contact stress distributions were based on the contact stress measurements under heavy aircraft tire load reported by Rolland [6]. In the longitudinal direction, a half-sinusoidal pressure distribution was assumed along the contact length of each rib. The peak contact stresses beneath two edge ribs were assumed equal to 2.5 times the tire inflation pressure; while the peak contact stresses under central ribs were assumed equal to 1.2 times the tire inflation pressure. As the inflation pressure increases, the contact length decreases; while the contact width was assumed constant due to the relatively high lateral stiffness of the tire sidewall. Table 1 summarizes the contact stress distributions and contact areas under loading of 273kN,

respectively, at tire inflation pressure of 1.45MPa (210psi) and 1.69MPa (245psi). The contact area was estimated from the tire imprint measurement at NAPTF.

Table 1. Contact Stress Distributions and Contact Areas (Tire load: 272.7kN [61.3kips]).

Tire	Contact width (mm)/(inch)	Tire pressure: 1.45MPa (210psi)		Tire pressure: 1.69MPa (245psi)	
		Length (mm)/(inch)	Peak stress (MPa)/(psi)	Length (mm)/(inch)	Peak stress (MPa)/(psi)
Rib 1	60/2.4	520/20.5	3.63/526	440/17.3	4.32/613
Rib 2	50/2.0	520/20.5	1.74/252	440/17.3	2.11/306
Rib 3	120/4.7	520/20.5	1.74/252	440/17.3	2.11/306
Rib 4	50/2.0	520/20.5	1.74/252	440/17.3	2.11/306
Rib 5	60/2.4	520/20.5	3.63/526	440/17.3	4.23/613
Groove	15/0.6	520/20.5	0	440/17.3	0

3D FE MODEL

A 3-D FE model was built to predict pavement responses under moving tire loading at different load and pressure levels. The schematic illustration of the FE mesh is shown in Fig. 5. In the FE model, the element thicknesses were selected at 10-20 mm (0.4-0.8inch) for the HMA layers and 30-50mm (1.2-2inch) for the base/subbase layers and subgrade. Infinite elements were used in the transverse and longitudinal boundaries of the model and at the bottom of subgrade to reduce the degrees of freedom at far field and absorb stress waves for dynamic analysis. The Coulomb friction model was used at the interface between each adjacent layer and the coefficient of friction is assumed as 1.0 [13].

The loading area at a specific level of load and inflation pressure was considered by adjusting the numbers and dimensions of elements within the tire imprint area. The widths of the elements within the loading area were selected at 10-25mm (0.4- 1inch) depending on the widths of tire ribs and grooves. The lengths of the elements were selected at 40 mm in the longitudinal (trafficked) direction. The elements in the loading area were loaded with the non-uniform contact stress corresponding to their locations within the tire imprint area. For the non-uniform stress distribution, the loading magnitudes of contact stress continuously changed at each step as the tire was moving. The dynamic transient analysis was used in this study considering the inertia associated with the moving load and the dependency of the material properties on the loading frequency. Additional details about the 3-D FE model, tire contact stress, moving load simulation and dynamic transient analysis can be found elsewhere [14, 15].

A sensitivity analysis was conducted to determine the location of infinite boundaries and the loading area in the finite domain of the 3-D FE model. After comparing the tensile and shear strains in the asphalt layer, the finite dimension of the model was selected to be 5.4 m (17.7ft) (length) \times 3.4m (11.2ft) (width) \times 2.6m (8.5ft) (depth) with an in-plane loading area of 2.8 \times 0.7m (9.2 \times 2.3ft) to balance the computation cost and accuracy.

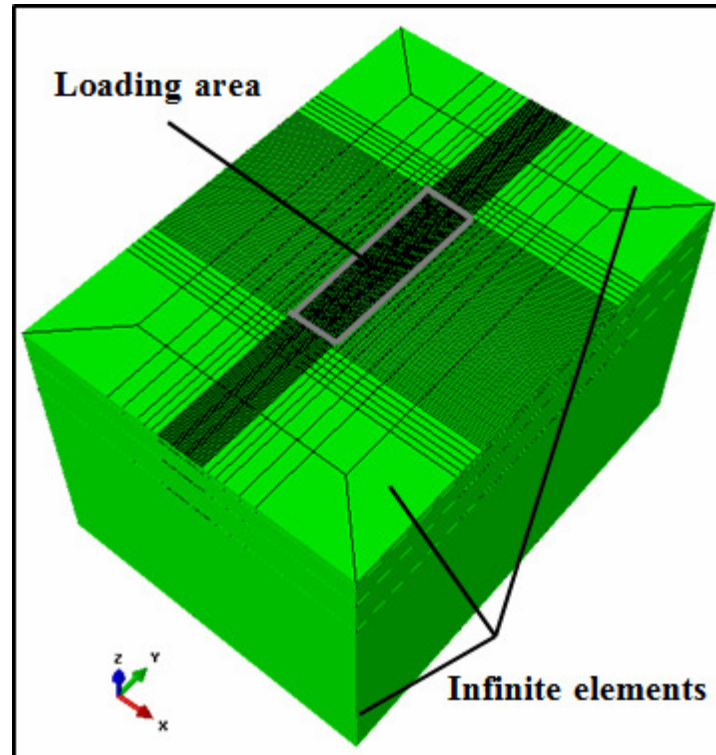
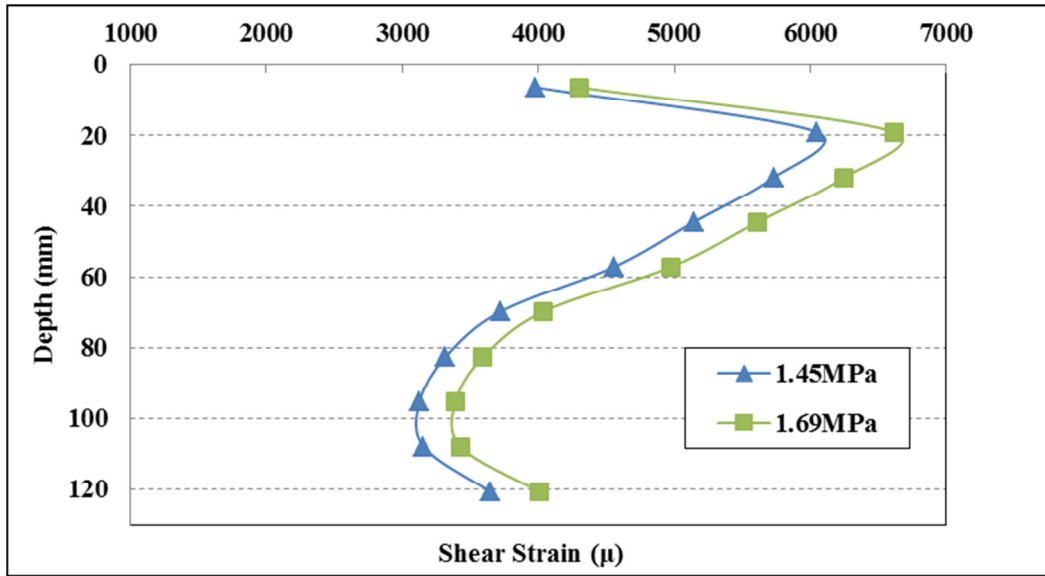


Figure 5. Schematic Illustration of FE Mesh.

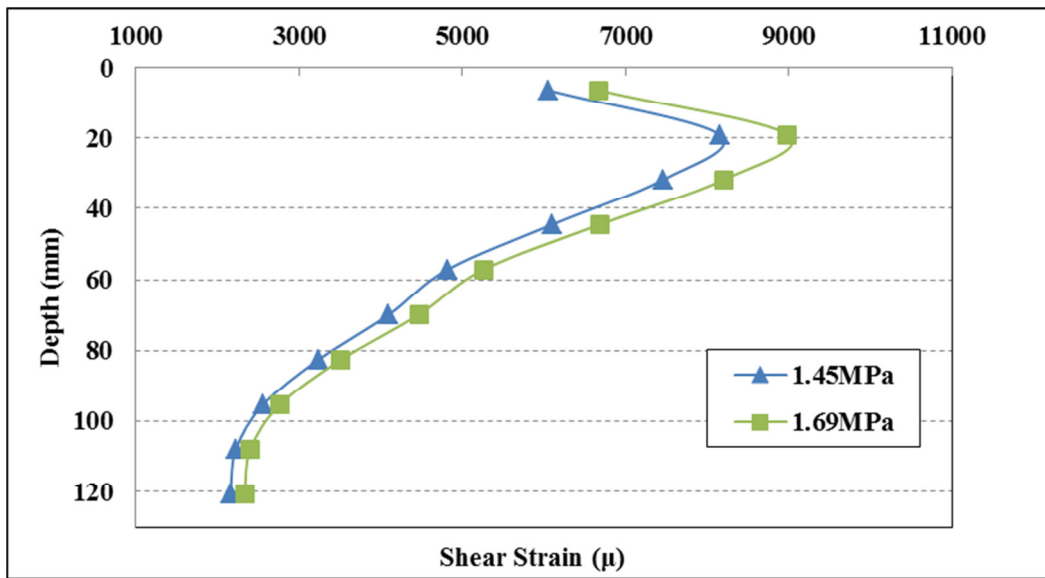
RESULTS AND ANALYSIS

The critical responses considered in this study included the tensile strain at the bottom of the HMA layer that is responsible for the bottom-up fatigue cracking, and the shear strains and compressive strains in the HMA layer that are responsible for rutting and near-surface cracking. Although different speeds can be simulated in the developed models, all the pavement responses were calculated at tire moving speed of 1.1km/h (1ft/s) that was used in the full-scale test.

The in-depth distributions of shear strains and compressive strains are as plotted in Figs. 6 and 7, respectively. The critical shear strain was located at the shallow-depth of the asphalt layer; while the critical compressive strain was located at the surface of asphalt layer. The strain responses under the measured temperature profile are smaller than the ones under the reversed temperature profile. However, the strain distribution patterns along the pavement depth are similar for both temperature profiles.

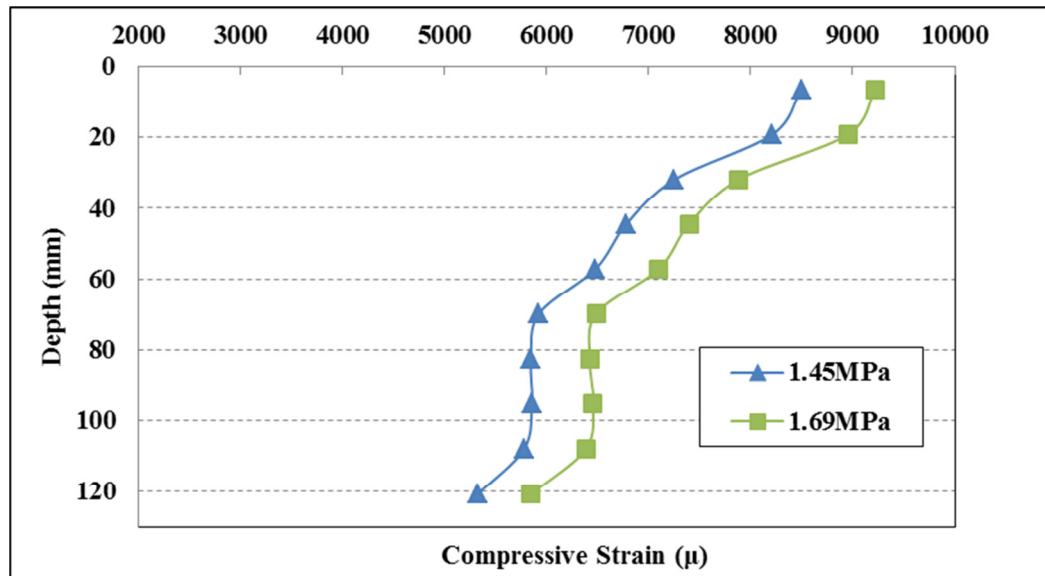


(a)

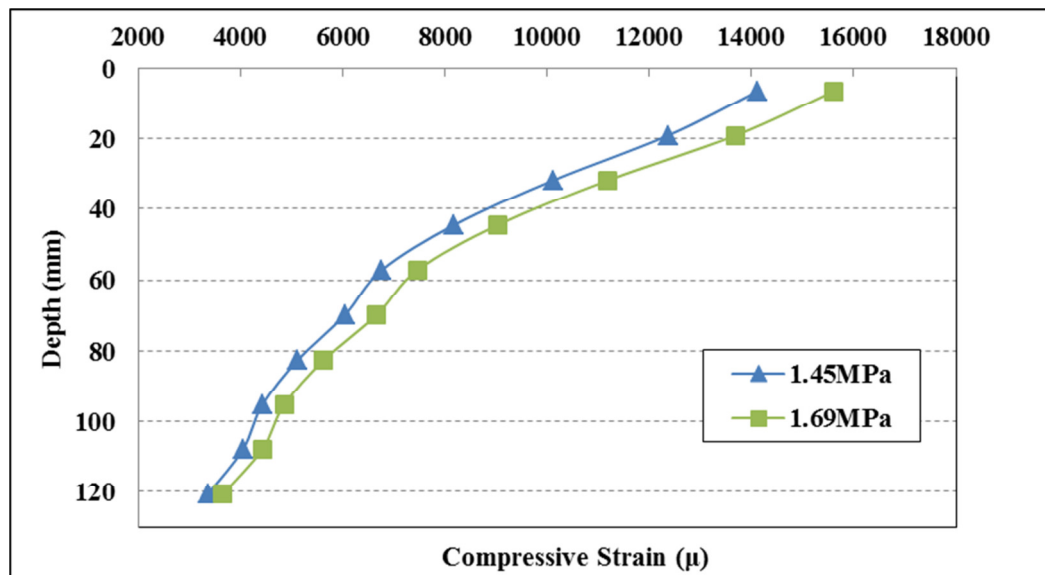


(b)

Figure 6. In-depth Distributions of Shear Strains Using the (a) Measured and (b) Reversed Temperature Profiles (Tire load: 272.7kN [61.3kips]).



(a)



(b)

Figure 7. In-depth Distributions of Compressive Strains Using the (a) Measured and (b) Reversed Temperature Profiles (Tire load: 272.7kN [61.3kips]).

Table 2 summarizes the maximum pavement responses at different tire pressure levels using the measured and reversed temperature profiles. Compared to the tire pressure of 1.45MPa (210psi), the higher tire pressure of 1.69MPa (245psi) induces 22-25% greater maximum longitudinal (critical) tensile strain at the bottom of the HMA layer. This is probably because the higher tire inflation pressure causes the greater tire contact stresses in the contact area. It indicates that increasing tire inflation pressure would reduce the service life of airfield pavements by inducing the greater fatigue cracking potential. In the real airfield pavement practice, bottom-up fatigue cracking potential decreases significantly as the thickness of asphalt

layer increases. Therefore near-surface rutting or cracking caused by compressive strains and shear strains becomes more critical.

The results show that the increase of tire inflation pressure from 1.45MPa (210psi) to 1.69MPa (245psi) causes 9-11% greater maximum shear strains and compressive strains. On the other hand, the higher tire inflation pressure causes 18% greater maximum deviator stresses. Interestingly, the effect of high tire pressure on maximum strain responses keeps the similar trends in both temperature profiles. It indicates that although the magnitudes of maximum strain responses vary depending on the temperature profile in the HMA layer, the changes of maximum strain responses due to tire pressure are not affected by temperature variation.

Table 2. Comparison of Pavement Responses at Different Tire Pressures

Tire load: 272.7kN (61.3 kips)	Measured Temperature Profile			Reverse Temperature Profile		
	1.45 (210)	1.69 (245)	Change	1.45 (210)	1.69 (245)	Change
Tire pressure: MPa (psi)						
Critical tensile strain (μ)	1068	1339	+25%	899	1101	+22%
Shear strain (μ)	6049	6617	+9%	8158	8991	+10%
Compressive strain (μ)	8496	9225	+9%	14119	15614	+11%
Deviator Stress (kPa [psi])	2107 (305)	2489 (361)	+18%	1823 (264)	2154 (312)	+18%

The rutting depths in the HMA layer were calculated using two mechanistic-empirical (M-E) transfer functions proposed by AASHTO Mechanistic-Empirical Pavement Design Guide (MEPDG) and Asphalt Institute (AI), Eq. 4, 5 and 6 [16, 17]. All calibration parameters in these models were based on the global calibration as recommended. The rutting depth after 400 and 800 loading cycles were calculated and the results are shown in Table 3.

Considering two temperature profiles, the influence of high tire pressure on the rutting depths using the MEPDG model are similar to the effect observed from the AI model. However, the absolute magnitude of rutting depth in the AI model is much greater than in the MEPDG model under the same loading conditions. It is probably because the compressive strain is a predominant factor in the MEPDG model. Instead, the deviator stress and other material properties were used in the AI model in addition to the compressive strain. This trend is consistent with the findings reported from another study [18]. In general, the high tire inflation pressure loading causes slightly greater rutting depth when assuming the vertical compression and consolidation are the major causes of rutting in the HMA layer.

$$\text{Log} \left(\frac{\varepsilon_p}{\varepsilon_r} \right) = -3.35 + \text{Log}(K_Z) + 1.56\text{Log}(T) + 0.48\text{Log}(N) \quad (4)$$

where:

ε_p is plastic strain calculated at the mid-depth of a thickness increment;

ε_r is incremental resilient strain at the mid-depth of a thickness increment;

T is temperature at the mid-depth of a thickness increment, °F;

N is number of axle load applications of a specific axle type; and

K_Z is depth function

$$\begin{aligned} \text{Log}\left(\frac{\varepsilon_p}{\varepsilon_r}\right) = & -6.631 + 0.4354\text{Log}(N) + 2.767\text{Log}(T) + 0.11\text{Log}(\sigma_d) \\ & -0.118\text{Log}(\eta) + 0.93\text{Log}(V_{beff}) + 0.501\text{Log}(V_a) \end{aligned} \quad (5)$$

where;

σ_d is deviator stress, psi;

η is viscosity of the asphalt binder at 70°F, 0.366×10^6 poise here;

V_{beff} is effective asphalt content by volume, 9.4% here; and

V_a is air void volume, 4% here.

$$RD_{AC} = \sum_{i=1}^N (\varepsilon_p)_i \Delta h_i \quad (6)$$

where,

RD_{AC} is rutting depth at the asphalt concrete layer;

N is number of sub-layers;

$(\varepsilon_p)_i$ is vertical plastic strain at mid-thickness of layer i ; and

Δh_i is thickness of sublayer i .

Table 3. Comparison of Rut-Depths at Different Tire Pressures.

Tire load: 272.7kN (61.3kips)	AI Model			MEPDG model		
Tire pressure: Mpa (psi)	1.45 (210)	1.69 (245)	Change	1.45 (210)	1.69 (245)	Change
Rutting depth (in.)	Measured temperature profile at NAPTF					
400 th cycle	1.40	1.56	+11%	0.65	0.71	+9%
800 th cycle	1.90	2.11	+11%	0.91	1.00	+10%
Rutting depth (in.)	Reversed temperature profile					
400 th cycle	1.55	1.74	+12%	0.77	0.85	+10%
800 th cycle	2.09	2.35	+12%	1.08	1.19	+10%

CONCLUSIONS

In this study, airfield pavement responses under different aircraft loading conditions are calculated and compared using a 3-D FE model considering two different temperature profiles. The results show that the high tire pressure causes greater responses by different percentages. The increase of tire pressure from 1.45MPa (210psi) to 1.69MPa (245psi) induces 22-25% greater longitudinal (critical) tensile strain at the bottom of the HMA layer. In near-surface area, the high tire inflation pressure causes 9-11% greater shear and compressive strains and 18% greater deviator stresses. Although the magnitudes of maximum strain responses vary depending

on the temperature profile in the HMA layer, the changes of maximum strain responses due to tire pressure are not affected by temperature variation. In general, the high tire inflation pressure loading causes slightly greater rutting depth when assuming the vertical compression and consolidation are the major causes of rutting in the HMA layer.

ACKNOWLEDGMENT

The authors would like to acknowledge Federal Aviation Administration for providing funding support of the research. The contents of the paper reflect the views of the authors, who are responsible for the facts and accuracy of the data presented within. The contents do not necessarily reflect the views and policies of the FAA. This paper does not constitute a standard, specification or regulation.

REFERENCES

1. Machemehl, R.B., Wang, F., and Prozzi, J.A., "Analytical Study of Effects of Truck Tire Pressure on Pavements with Measured Tire-Pavement Contact Stress Data," *Transportation Research Record No. 1919*, TRB, Washington, D.C., pp. 111-120, 2005.
2. ICAO, *Aerodrome Design Manual*, Part 3, Pavements, 2nd edition, Document 9157-AN/901, International Civil Aviation Organization, 1983.
3. Howell, W.E., Perez, S.E., and Vogler, W.A., "Aircraft Tire Footprint Forces," *ASTM Special Technical Publication (SPT) 929*, pp. 110-124, 1986.
4. Tielking, J.T., and Abraham, M.A., "Measurement of Truck Tire Footprint Pressures," *Transportation Research Record No. 1435*, TRB, Washington, D.C., pp. 92-99, 1994.
5. Daugherty, R.H., "A Study of the Mechanical Properties of Modern Radial Aircraft Tires," NASA Langley Research Center, 2003.
6. Rolland, E., "Tire Pressure Test Effect on Pavement," Airbus High Tire Pressure Workshop (in CD), Toulouse, France, 2009.
7. Garg, N., "Post-traffic Testing at the National Airport Pavement Test Facility: Test Item MFC," Technical Note to Federal Aviation Administration, Galaxy Scientific Corporation, 2001.
8. Hayhoe, G.F. and Garg, N., "Subgrade Strains Measured in Full-scale Traffic Tests with Four- and Six-wheel Landing Gears," Proceedings of 2002 FAA Airport Technology Transfer Conference (in CD), Atlantic City, NJ, 2002.
9. Garg, N. and Hayhoe, G.F., "Asphalt Concrete Strain Responses at High Loads and Low Speeds at the National Airport Pavement Test Facility (NAPTF)," Technical Report to FAA, Galaxy Scientific Corporation, 2001.
10. Roginski, M.J., "Effects of Aircraft Tire Pressures on Flexible Pavement," Proceedings of the International Conference on Advanced Characterization of Pavement and Soil Engineering, Athens, Greece, pp 1473-1481, 2007.
11. Fabre, C., Balay, J.M., and Lerat, P., "Full-Scale Aircraft Tire Pressure Tests," Proceedings of 2010 FAA Worldwide Airport Technology Transfer Conference (in CD), Atlantic City, NJ, 2010.
12. Ferry, J.D. *Viscoelastic Properties of Polymers*, John Wiley & Sons, Hoboken, NJ, USA, 1980.

13. Romanoschi, S.A. and Metcalf, J.B., "Effects of Interface Condition and Horizontal Wheel Loads on the Life of Flexible Pavement Structures," *Transportation Research Record*, No. 1778, TRB, Washington D.C., pp. 123-131, 2001.
14. Al-Qadi, I.L., Wang, H., Yoo, P.J., and Dessouky, S.H., "Dynamic Analysis and In-Situ Validation of Perpetual Pavement Response to Vehicular Loading," *Transportation Research Record*, No. 2087, TRB, Washington, D.C., pp. 29-39, 2008.
15. Wang, H. and Al-Qadi, I.L., "Combined Effect of Moving Wheel Loading and Three-Dimensional Contact Stresses on Perpetual Pavement Responses," *Transportation Research Record No. 2095*, TRB, Washington, D.C. pp. 53-61, 2009.
16. ARA, Inc., "Development of the 2002 Guide for the Design of New and Rehabilitated Pavements," NCHRP 1-37A Report, Transportation Research Board, 2004.
17. Leahy, R.B., *Permanent Deformation Characteristics of Asphalt Concrete*, Ph.D. Dissertation, University of Maryland, 1989.
18. Von Quintus, H., "Calibration of Rutting Models for HMA Structural and Mix Design," Final Report to Transportation Research Board of the National Academies, ARA, Inc., 2012.